PHYSICAL REVIEW B **108**, 155417 (2023)

Exciton many-body interactions and charge transfer in $CsPbBr_3$/graphene derivatives

Naresh Chandra Maurya,[1] Riyanka Karmakar,[1] Rajesh Kumar Yadav,[1] Pravrati Taank,[1] Santu K. Bera,[1]
Anirban Mondal,[1] Dipendranath Mandal,[1] Megha Shrivastava,[1] Md. Nur Hasan,[2] Tuhin Kumar Maji,[3]
Debjani Karmakar,[4,5] and K. V. Adarsh[1,*]

[1]*Department of Physics, Indian Institute of Science Education and Research Bhopal, Bhopal 462066, India*
[2]*Department of Chemical and Biological Sciences, S. N. Bose National Centre for Basic Sciences, Block JD, Sector III, Salt Lake, Kolkata 700106, India*
[3]*Department of Physics, Indian Institute of Science, Bangalore 560012, India*
[4]*Department of Physics and Astronomy, Uppsala University, Box 516, SE-75120 Uppsala, Sweden*
[5]*Technical Physics Division, Bhabha Atomic Research Centre, Mumbai 400085, India*

(Received 4 April 2023; revised 18 August 2023; accepted 29 September 2023; published 17 October 2023)

Charge separation and many-body interactions at the interface of the light-absorbing semiconductor and contact layer are of crucial importance to the photophysical properties and optoelectronic device performance. Here, we report the exciton many-body interactions and charge transfer dynamics at the interface of metal halide perovskite nanocrystals and graphene derivatives [graphene oxide (GO) and reduced GO (RGO)] using ultrafast transient absorption (TA) and time-resolved photoluminescence (PL) measurements. At the early timescales, the TA spectra of $CsPbBr_3$/GO and $CsPbBr_3$/RGO show an asymmetric derivative feature originating from the exciton many-body interactions. The band gap renormalization and binding energies of exciton and biexciton of $CsPbBr_3$ nanocrystals are significantly reduced in $CsPbBr_3$/GO(RGO) due to the charge transfer and change in the dielectric environment, respectively. More specifically, the exciton (biexciton) binding energy of $CsPbBr_3$ nanocrystals, originally 38 ± 2 (34 ± 1) meV, decreases to 27 ± 1 (22 ± 1) meV in $CsPbBr_3$/RGO and 17 ± 1 (15 ± 1) meV in $CsPbBr_3$/GO. Furthermore, we observe a reduction in the Auger recombination rate and exciton PL quenching in $CsPbBr_3$/GO and $CsPbBr_3$/RGO, corroborating the charge transfer mechanism. Our systematic studies successfully describe photoexcited charge transfer from $CsPbBr_3$ nanocrystals to GO (RGO) in 7.0 ± 0.4 (4.2 ± 0.1) ps, which is one order of magnitude faster than the charge transfer for other acceptor materials such as metal oxide, fullerene, anthraquinone, 1-aminopyrene, and phenothiazine. Our results offer insights and guidance for perovskite-based high-performance optoelectronic devices.

DOI: 10.1103/PhysRevB.108.155417

I. INTRODUCTION

Lead halide perovskite nanocrystals (LHPNs) of the general formula $CsPbX_3$ (X = Cl, Br, or I) are a relatively new class of low-dimensional semiconductors [1] that have generated significant research interest due to their exceptional potential in fundamental and device physics [2]. These nanocrystals (NCs) exhibit intriguing characteristics reminiscent of molecular systems, with customizable-atom-like features [3], strong band-edge exciton-photon coupling [4], a remarkably high photoluminescence (PL) quantum yield of near unity [1,5], and a unique exciton fine structure of fast-decaying bright triplet states below the dark singlet state [6]. Their electronic structure is characterized by complex defect-tolerant antibonding orbitals forming the valence band (VB) maximum and conduction band (CB) minimum [7], resulting in remarkably low trap densities (10^{10} cm^{-3}) even when synthesized at room temperature [8]. The defect-tolerant electronic structure of LHPNs is a key factor contributing to their long lifetimes (∼7 ns) [9] and substantial diffusion lengths (∼10 μm) [10]. A recent study on strongly confined $CsPbBr_3$ NCs reported PL from dark excitons with a microsecond lifetime [11]. As a consequence, these NCs have found versatile applications in optical and optoelectronic devices, including low-threshold lasing [12], light-emitting diodes [13], and solar cells [14]. Recently, it has been demonstrated that the LHPNs can host novel spin functionalities [6,15–19] due to the large spin-orbit coupling that provides clean spin-selection rules to optically prepare, manipulate, and measure the carrier spins and their populations [19,20]. Since LHPNs can meet the requirements of cost-effective synthesis protocols and easy integration with semiconductor devices in the existing nanoelectronics technology framework, they are therefore foreseen as the building blocks of next-generation semiconductor technology.

Notably, the Coulomb interactions between the charge carriers in LHPNs are remarkably strong, which is reflected in the high binding energies of the exciton (bound electron-hole pair), the biexciton (bound exciton pair), and other high-order exciton complexes such as the triexciton [18,21,22] similar to conventional semiconductor NCs [23–25]. We have recently demonstrated an unusually large Haynes factor (ratio of biexciton to exciton binding energy) of near unity in $CsPbBr_3$

---

[*] adarsh@iiserb.ac.in

NCs [18]. This remarkable result shows that the biexciton and exciton binding energies can be tuned to more than 100 meV by exploiting the quantum confinement effect [26], keeping the Haynes factor at unity. Moreover, the Haynes factor in LHPNs is found to be at least an order of magnitude larger than that observed in conventional low-dimensional semiconductors [18,27–29]. The enhanced Coulomb interactions due to low-dimensional confinement in LHPNs have also resulted in another intriguing effect known as band-gap renormalization (BGR). This many-body effect describes the reduction of the fundamental band gap with increasing free-carrier density [30]. In addition to the conventional BGR, we have recently demonstrated a giant spin-selective BGR of 57 ± 1 meV at room temperature in LHPNs [19]. It is well established that the strength of Coulomb interactions between charge carriers is influenced by the surrounding dielectric environment [31,32]. An increase in dielectric screening, for example, can reduce the electron-hole or electron-electron interactions, leading to a reduction in exciton and biexciton binding energies, thereby affecting the many-body interaction of the system. Theoretically, this opens up a new degree of freedom to engineer the exciton many-body interactions and the electronic band gap, which could have significant implications for optoelectronic applications, including quantum information processing and photovoltaic devices [19,33]. Analogous effects have been observed in atomically thin transition metal dichalcogenide heterostructures [34,35], and similar control and tuning of exciton complexes are highly desirable in LHPNs due to their dominant role in the optical response. This can also be achieved by optical carrier injection via ultrafast laser pulses [36,37]. Since the excitonic complexes dominate the optical response of LHPNs, the ability to control and tune them is of crucial importance to optoelectronic applications [38,39]. To this end, various methods have been explored, such as modifying the chemical composition [1,40–42], adjusting the quantum size [43], and exploring shape effects [44]. Nevertheless, interfaces between LHPNs and dielectric media, including graphene derivatives such as graphene oxide (GO) and reduced GO (RGO) [45–50], low-dimensional layered materials such as black phosphorus [51], Bi_2O_2Se [52], and transition metal dichalcogenides [53–55], are regarded as ideal platforms for studying charge transfer and associated changes in the optical response. Dielectric screening and charge transfer lead to the formation of the space-charge region, giving rise to unprecedented device architectures that include highly efficient solar cells [46]. Nevertheless, most previous studies on these interfaces primarily focused on the synthesis [45,47,48], charge transfer dynamics [48–50], and hot carrier extraction [56,57]. Needless to say, the concept of controlling the exciton and biexciton binding energy and many-body interactions has so far not been successfully demonstrated in the LHPN-dielectric interfaces, and furthermore, a fundamental understanding of these interfaces is still lacking.

In this paper, we comprehensively investigate exciton many-body interactions and charge transfer dynamics at the interface of $CsPbBr_3/GO$ and $CsPbBr_3/RGO$. Our studies reveal a significant reduction in exciton and biexciton binding energies of $CsPbBr_3$ NCs when interfaced with GO or RGO, owing to the modification of the dielectric environment. Furthermore, we observe a notable decrease in many-body interactions, such as BGR and the Auger recombination rate in $CsPbBr_3$ NCs, which we attribute to the ultrafast charge transfer occurring at the interfaces. Our systematic studies successfully describe photoexcited charge transfer from $CsPbBr_3$ NCs to GO (RGO), which occurs on an ultrafast timescale of 7.0 ± 0.4 (4.2 ± 0.1) ps. Notably, this charge transfer rate is one order of magnitude faster than that observed in other interfaces [58–61]. Furthermore, our density functional theory (DFT) calculations show strong electronic coupling and charge transfer. Remarkably, the quenching of excitons in $CsPbBr_3/GO$ and $CsPbBr_3/RGO$, as observed through PL and time-resolved PL measurements, concurs with the charge transfer route.

II. SAMPLE PREPARATION AND PHYSICAL CHARACTERIZATION

High-quality $CsPbBr_3$ NCs and GO were synthesized using the hot injection method and modified Hummer's method, respectively [62,63]. To obtain RGO from GO, thermal treatment was employed. The wet chemical synthesis was strategically designed based on a dispersible template-based hot injection method [64] to fabricate strongly coupled $CsPbBr_3/GO$ and $CsPbBr_3/RGO$; see Supplemental Material (SM) for details and a depiction in Fig. S1 [65]. For characterizing the morphology of the synthesized samples and confirming the presence of $CsPbBr_3$ NCs on graphene derivatives, high-resolution transmission electron microscopy (HRTEM) was utilized. The obtained images in Figs. S2(a)–S2(c) display the cubic morphology of $CsPbBr_3$ NCs, $CsPbBr_3/GO$, and $CsPbBr_3/RGO$ with an average edge length of 11 ± 1 nm. The size distribution of $CsPbBr_3$ NCs, $CsPbBr_3/GO$, and $CsPbBr_3/RGO$ can be observed in the size histograms shown in Figs. S3(a)–S3(c) of the SM [65]. Furthermore, the powder x-ray diffraction patterns of $CsPbBr_3$ NCs, $CsPbBr_3/GO$, and $CsPbBr_3/RGO$ (Fig. S4) provide evidence for the formation of interfaces between $CsPbBr_3$ NCs and GO or RGO. Samples were dispersed in toluene for all spectroscopic investigations reported in this paper.

III. RESULTS AND DISCUSSION

A. Coulomb engineering of exciton and biexciton binding energy

The attractive Coulomb interaction between electrons and holes leads to the formation of exciton states below the electronic band-gap energy E_g, and the difference between E_g and the exciton resonance energy E_0 defines the exciton binding energy E_b. To get insight into E_b under different dielectric backgrounds, we have recorded the optical absorption spectrum of $CsPbBr_3$ NCs, $CsPbBr_3/GO$, and $CsPbBr_3/RGO$ [Figs. 1(a)–1(c)]. The nearly same absorbance of $CsPbBr_3$, $CsPbBr_3/RGO$, and $CsPbBr_3/GO$ ensures the same concentration of $CsPbBr_3$ NCs in all samples. The spectrum consists of a sharp exciton peak followed by a saturation due to continuum bands, which are separated by using Elliott's model [66] [Eq. (S1)] for the direct band-gap semiconductor (details in the SM [65]). We obtained the E_b as 38 ± 2, 27 ± 1, and 17 ± 1 meV for $CsPbBr_3$, $CsPbBr_3/RGO$, and $CsPbBr_3/GO$, respectively. The blueshift in E_0 along with the slight redshift

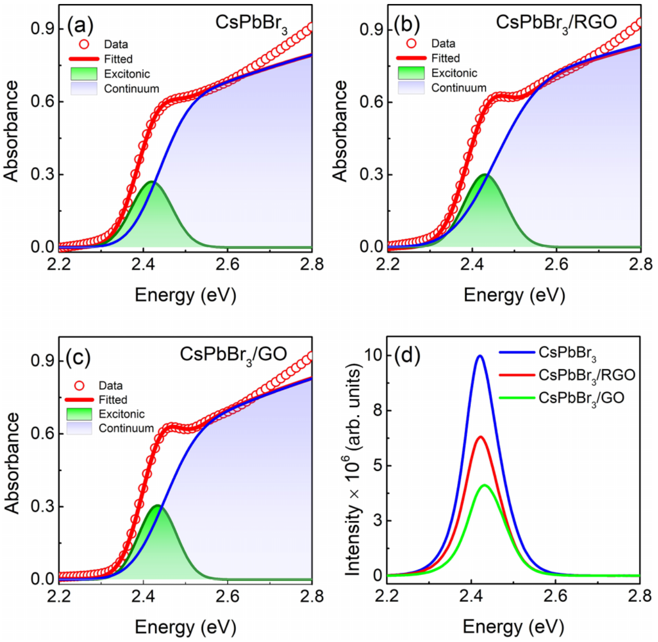

FIG. 1. Ground state optical absorption spectrum and theoretical fit using Elliott's model for (a) $\mathrm{CsPbBr_3}$ NCs, (b) $\mathrm{CsPbBr_3/RGO}$, and (c) $\mathrm{CsPbBr_3/GO}$. The exciton resonance and continuum absorptions are depicted in green and blue, respectively. (d) Steady-state PL spectra for 3.10 eV excitation energy. The gradual blueshift of the PL peak (quenching of PL intensity) in $\mathrm{CsPbBr_3/GO}$ and $\mathrm{CsPbBr_3/RGO}$ compared with $\mathrm{CsPbBr_3}$ NCs suggests the change in dielectric environment (charge transfer).

in E_g (details in the SM [65], Table S1) of $\mathrm{CsPbBr_3/GO}$ and $\mathrm{CsPbBr_3/RGO}$ compared with $\mathrm{CsPbBr_3}$ NCs results in an overall reduction of the E_b, which is due to the screening of the Coulomb interaction by the dielectric environment. Furthermore, the dielectric constant of GO ($\sim 10^4 - 10^6$) is greater than that of RGO ($\sim 10^2 - 10^3$), which screens the Coulomb potential, resulting in the lower E_b in $\mathrm{CsPbBr_3/GO}$ compared with $\mathrm{CsPbBr_3/RGO}$ [67–71]. Such type of behavior has already been reported in various types of interfaces [34,35]. To get further evidence of the blueshift of E_0 with the change in the dielectric environment, we have performed the steady-state PL measurements by exciting the samples at 3.10 eV under ambient conditions, and corresponding results are presented in Fig. 1(d). The exciton PL from $\mathrm{CsPbBr_3}$ NCs is centered at 2.420 ± 0.001 eV, which exhibits a full width at half maximum (FWHM) of 95 ± 1 meV. In contrast, in $\mathrm{CsPbBr_3/RGO}$, this PL blueshift is to 2.423 ± 0.001 eV, with a FWHM of 97 ± 1 meV. Similarly, in the case of $\mathrm{CsPbBr_3/GO}$, the PL shows a blueshift to 2.433 ± 0.003 eV, with a FWHM of 102 ± 2 meV. This behavior is precisely similar to the results that we have obtained from optical absorption measurements. Another important result we notice is that there is a significant reduction in the PL intensity of $\sim 59\%$ ($\sim 37\%$) for $\mathrm{CsPbBr_3/GO}$ ($\mathrm{CsPbBr_3/RGO}$). Since there is neither a new PL peak nor overlapping absorption, we ruled out the energy transfer mechanism [49]. Therefore we attribute the PL quenching to the photoexcited charge transfer between the $\mathrm{CsPbBr_3}$ NCs and GO or RGO. This is in line with the shifts of E_b and E_0, as evidenced from the optical absorption. Although GO and RGO are suitable acceptors, the higher capacity of GO to consume more charges is due to its oxidation state [72], leading to higher PL quenching of $\mathrm{CsPbBr_3/GO}$.

The biexciton binding energy is determined through spectrally resolved ultrafast transient absorption (TA) spectroscopy [73]. More details can be found in the SM [65]. Our experimental setup involved exciting the samples using 120-fs pulses centered at 3.10 eV, which is ~700 meV higher than the band-gap energy of the samples. The resulting change in absorbance spectrum ($\Delta A = A_e - A_g$), where A is the absorbance and subscripts e and g refer to the excited and ground states, respectively, is measured using a probe pulse within the photon energy of 2.1–2.8 eV. Since we excite the samples with the above-band-gap-energy photons, the TA data have contributions from both excitons and free carriers. Taking this into consideration, we have modeled the TA data using Eq. (1):

$$\Delta A = \Delta A_{\mathrm{ex}} + \Delta A_{\mathrm{JDOS}}. \tag{1}$$

Here, $\Delta A_{\mathrm{ex}} = B \times A_g \mathrm{e}^{-(\frac{x-E_0-E_b'}{\Gamma_{0_e}})^2} - A_g \mathrm{e}^{-(\frac{x-E_0}{\Gamma_{0_g}})^2}$ and $\Delta A_{\mathrm{JDOS}} = A_{c_e}(E; E_c - \Delta E, \Gamma_c)[1 - f_e^q(E; E_f^q, T_c, \Gamma_{c_e})]^2 - A_{c_g}(E; E_c, \Gamma_{o_g})$ due to the shift in the joint density of states (JDOS). In these equations, B, A_g, E_0, Γ_0, E_b', E_c, A_c, ΔE, E_f^q, f_e^q, Γ_c, and T_c refer to the reduction in oscillator strength, the amplitude of the ground state absorption, the exciton position, the spectral width, the biexciton binding energy, the band gap, the continuum contribution, the free-carrier-induced redshift, the quasi-Fermi energy, the Fermi distribution function, the spectral width of continuum, and the carrier temperature, respectively. The subscripts e and g denote excited and ground states, respectively. A systematic investigation was conducted at different fluences to discern the contributions arising from excitons and free carriers. Specifically, measurements were performed well below the Mott density regime, where the system predominantly exhibits excitonic characteristics, and significantly above the Mott density, leading to a dominant electron-hole plasma behavior.

Figures 2(a)–2(c) depict contour plots and cross sections of the TA signals for $\mathrm{CsPbBr_3}$ NCs, $\mathrm{CsPbBr_3/GO}$, and $\mathrm{CsPbBr_3/RGO}$ at a fluence of $25\,\mu\mathrm{J/cm^2}$. At such low fluence, the system is characterized by its excitonic nature, with minimal contributions from the background BGR. The observed asymmetric derivative feature is a consequence of the Coulombic interaction between the optically excited hot excitons and the probe excitons, causing a redshift in the exciton resonance energy [74]. This is manifested in the TA spectrum as an asymmetric derivative feature, i.e., a negative signal (photobleach) at the exciton energy and photoinduced absorption on the lower-energy side of the exciton [75]. We initially assume that the impact of state filling on the band-edge signals is negligible during this early time, as the low-energy states remain unoccupied. However, as the time delay Δt is increased, the pump-generated hot exciton loses its excess energy and undergoes relaxation towards the band edge, leading to the derivative feature's disappearance, i.e., photoinduced absorption vanishes, and a bleach emerges at the exciton position due to state filling. This contributes to the

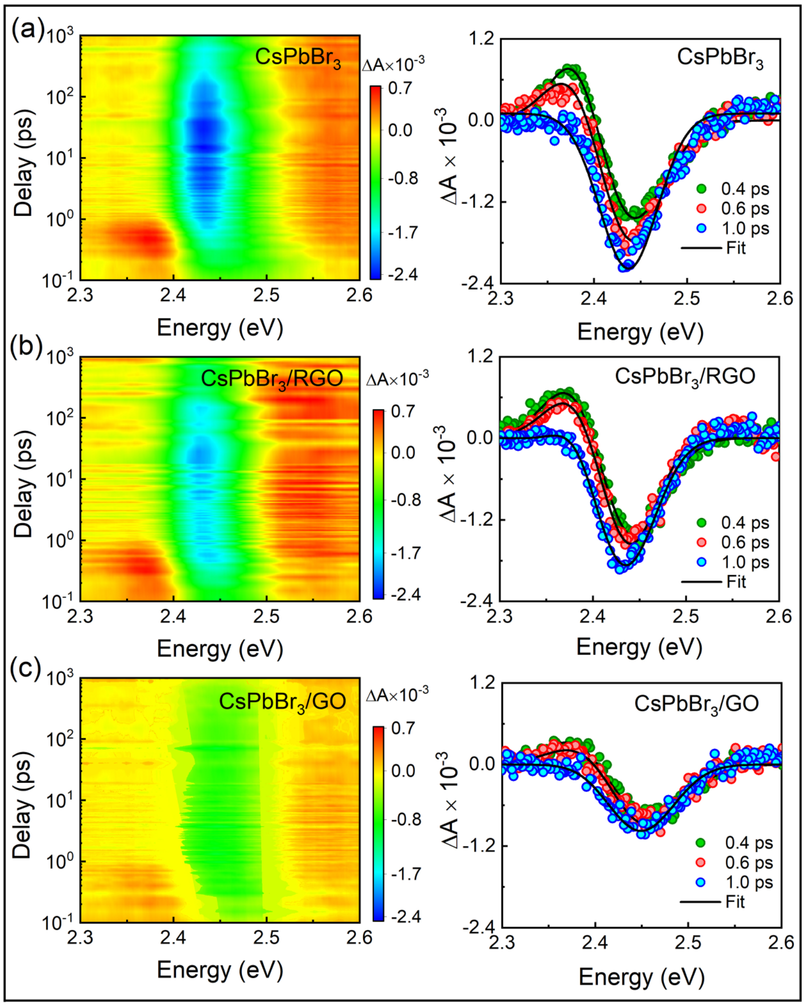

FIG. 2. Contour plots of the TA spectrum at 25 μJ/cm^2 pump fluence for (a) CsPbBr$_3$ NCs, (b) CsPbBr$_3$/RGO, and (c) CsPbBr$_3$/GO interfaces, along with the corresponding cross sections at different probe delays. The solid black curves are the fits. Early-timescale kinetics of the bleach and photoinduced absorption show a correlation between them for (d) CsPbBr$_3$ NCs, (e) CsPbBr$_3$/RGO, and (f) CsPbBr$_3$/GO interfaces. The solid curves represent the single exponential fit.

overall bleaching via Pauli blocking, and more importantly, induced absorption is replaced by band-edge bleach.

To accurately model the TA spectrum during this stage, we consider the excitonic contribution from Eq. (1), denoted as ΔA_{ex}. This enables us to extract the biexciton binding energy. Further details can be found in the SM [65]. Notably, the solid curves in Figs. 2(a)–2(c) correspond to the representative fits that match very well with the experimental data for all samples. Our analysis reveals biexciton binding energies of 15 ± 1, 22 ± 1, and 34 ± 1 meV for the CsPbBr$_3$/GO, CsPbBr$_3$/RGO, and CsPbBr$_3$ NCs, respectively [Figs. S5(a)–S5(f)]. The observed reduction in the biexciton binding energy at the interfaces can be attributed to the screening of the Coulombic interactions, as supported by our optical absorption and PL measurements. The decreased availability of carriers due to charge transfer may also contribute to this effect.

We estimated the intraband cooling time from the decay of the photoinduced absorption below the exciton resonance position at ~2.37 eV and the bleach buildup time at ~2.44 eV due to the state filling when carriers relax into the band edges [Figs. 2(d)–2(f)]. The average values of the intraband cooling time obtained from the single exponential fit of the photoinduced absorption decay and bleach buildup time of CsPbBr$_3$/GO, CsPbBr$_3$/RGO, and CsPbBr$_3$ NCs are 0.35 ± 0.02, 0.48 ± 0.02, and 0.55 ± 0.01 ps, respectively.

B. Many-body interactions: Band-gap renormalization and Auger recombination

After successfully demonstrating the TA features in the excitonic regime, we next turned our attention to the nature of the electron-hole plasma regime when the carrier density is above the Mott density. As we increased the pump fluence, the photobleach associated with the exciton transition experienced a blueshift and broadening as shown in the contour plots in Figs. 3(a)–3(c), eventually causing the suppression of the exciton resonance [Figs. 3(d)–3(f)], which indicates a transition from an excitonic regime to an electron-hole plasma regime. Additionally, we found that beyond a critical fluence (474 μJ/cm^2), the excitonic bleach saturation occurred, signifying a Mott transition [Figs. 3(g)–3(i)].

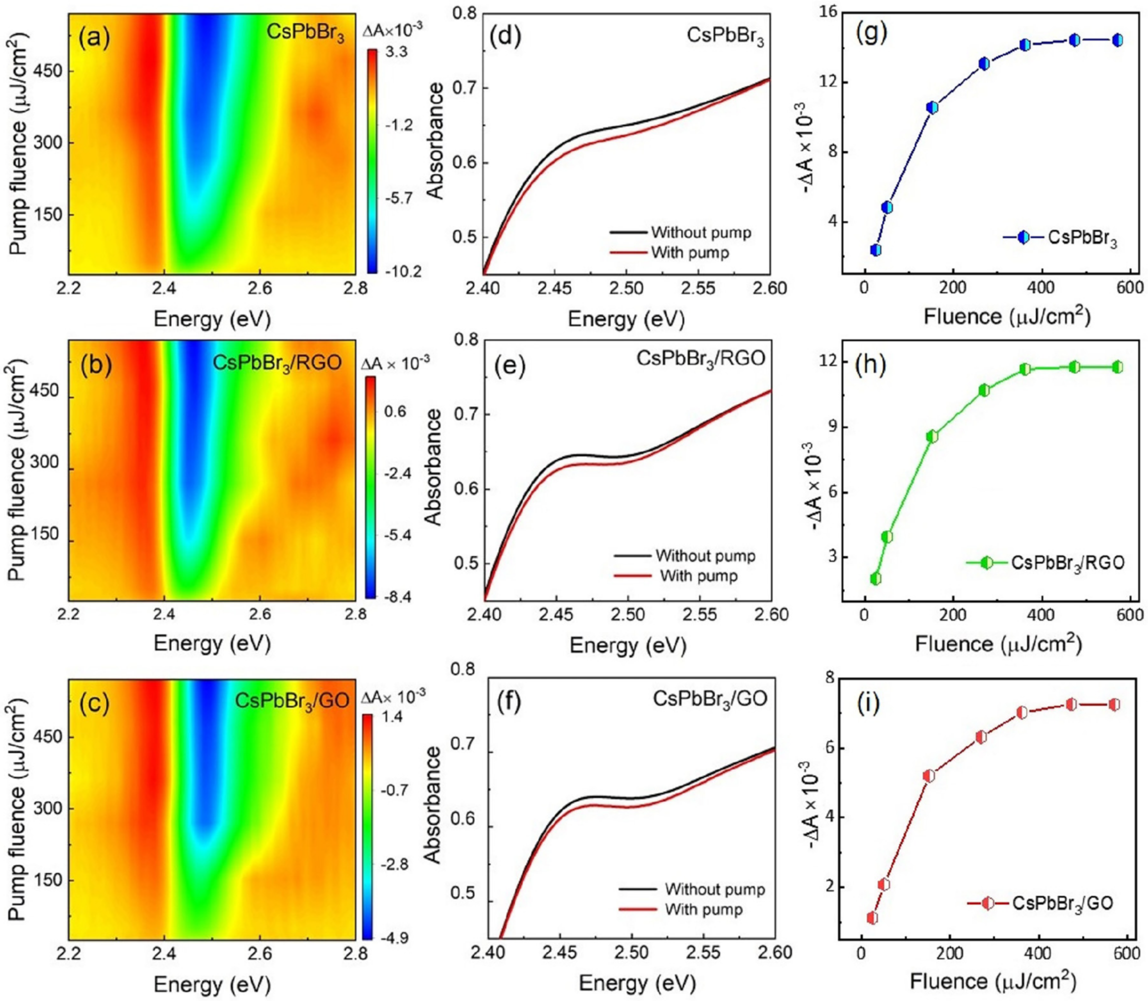

FIG. 3. Contour plots of the TA spectrum as a function of pump fluence showing the transition from an excitonic regime to an electron-hole plasma regime in (a) $CsPbBr_3$ NCs, (b) $CsPbBr_3$/RGO, and (c) $CsPbBr_3$/GO interfaces. The optical absorption spectra without (black) and with (red) pump showing the suppression of exciton absorption of (d) $CsPbBr_3$ NCs, (e) $CsPbBr_3$/RGO, and (f) $CsPbBr_3$/GO interfaces. Variation of exciton bleach amplitude with pump fluence showing the saturation of bleach in the high-fluence regime of (g) $CsPbBr_3$ NCs, (h) $CsPbBr_3$/RGO, and (i) $CsPbBr_3$/GO interfaces. These observations highlight the Mott transition from excitonic regime to conducting electron-hole plasma. The solid curves are guides to the eye.

To model TA at a higher excitation fluence and quantitatively correlate the spectra with BGR, we employed the ΔA_{JDOS} component of Eq. (1). The initial state of the JDOS with band-gap energy E_g ("JDOS initial") is schematically depicted in Figs. 4(a)–4(c), illustrating the carrier distribution characterized by a high temperature T_c determined by ($\hbar\omega - E_g$) and quasi-Fermi energy E_f^q describing carrier populations in the VB and CB. Pump-induced excited carriers result in a band-gap reduction, causing a redshift of the "JDOS initial" ["JDOS shifted" in Figs. 4(a)–4(c)] and subsequently leading to BGR. Carrier occupancy of the shifted JDOS is obtained by multiplying with the Fermi distribution ("JDOS occupied"). The TA spectrum corresponding to the continuum states, as defined by Eq. (1), displays broad bleach and photoinduced absorption on both energy sides, higher (2.6–2.8 eV) and lower (2.2–2.4 eV), as illustrated in the lower panels of Figs. 4(a)–4(c). This provides a clear signature of BGR driven by charge carrier accumulation. By fitting the cross-section spectra at $\Delta t = 0.4$ ps (Fig. S6), we calculated that the BGR values of $CsPbBr_3$, $CsPbBr_3$/RGO, and $CsPbBr_3$/GO using Eq. (1) are 107 ± 4, 90 ± 3, and 70 ± 3 meV, respectively. Remarkably, the pronounced reduction in BGR at the interfaces suggests efficient charge transfer from $CsPbBr_3$ to GO or RGO, consistent with our earlier discussions. Considering the known scaling of BGR with $n^{1/3}$ (where n is the carrier density) [75], our results indicate that for a given pump fluence, $CsPbBr_3/GO < CsPbBr_3/RGO < CsPbBr_3$, highlighting the superior charge acceptance capacity of GO compared with RGO.

After demonstrating a significant reduction in BGR at the interfaces due to charge transfer, we now turn our attention to Auger recombination: a nonradiative recombination channel in which the exciton transfers its energy to a third particle that is reexcited to a higher energy state [38,75,76]. To estimate the Auger recombination, we have compared TA decay curves of $CsPbBr_3$, $CsPbBr_3$/RGO, and $CsPbBr_3$/GO for different pump fluences in Figs. S7(a)–S7(c). The faster bleach recovery with increased excitation fluence can be associated

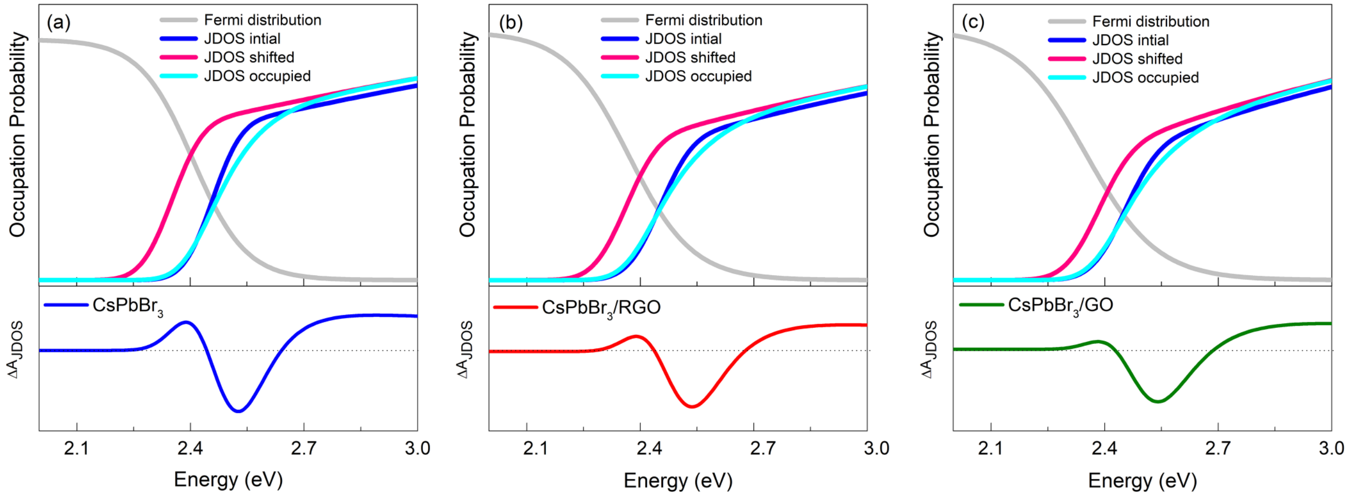

FIG. 4. Joint density of states (JDOS) and quasi-Fermi level for (a) $CsPbBr_3$ NCs, (b) $CsPbBr_3$/RGO, and (c) $CsPbBr_3$/GO interfaces. The data are obtained from calculations using Eq. (1), and the lower panels represent the TA spectrum corresponding to the continuum states.

with the nonradiative Auger recombination process [38,76]. To elucidate the recombination mechanism and Auger rate constants, we used the following rate equation [44,77]:

$$\frac{dn}{dt} = -(C_1 n + C_2 n^2 + C_3 n^3), \tag{2}$$

where C_1, C_2, and C_3 are first-order, second-order, and third-order rate constants, respectively. We find that the recombination primarily follows a second-order process over the entire range of excitation fluences [44]. Taking only the square term of Eq. (2), the second-order rate constant can be written as

$$\frac{n_0}{n_t} - 1 = C_2 n_0 t, \tag{3}$$

where n_0 and n_t are the initial carrier density and carrier density at time t, respectively. The left-hand side of Eq. (3) is plotted in Figs. 5(a)–5(c) as a function of time for various pump fluences. From the slope of the linear fit [Figs. 5(a)–5(c)] the second-order nonradiative rate constants are calculated as $(1.80 \pm 0.01) \times 10^{-6}$, $(1.71 \pm 0.01) \times 10^{-6}$, and $(1.60 \pm 0.01) \times 10^{-6}$ cm^{-3}/s for $CsPbBr_3$, $CsPbBr_3$/RGO, and $CsPbBr_3$/GO, respectively. It is interesting to notice here that the Auger rate constant reduces in the interfaces compared with $CsPbBr_3$. The possible reasons for the reduction of the Auger rate constant in the interfaces are as follows: (i) An increase in dielectric screening reduces the Coulomb interactions, and (ii) charge transfer from the $CsPbBr_3$ to GO or RGO increases the spatial separation of carriers due to reduced carrier density.

C. Charge transfer

To unlock the charge transfer rate, we measured the PL decay kinetics of $CsPbBr_3$, $CsPbBr_3$/RGO, and $CsPbBr_3$/GO at their respective emission maximum energy using time-resolved [78] PL [Fig. 6(a)]. More details can be found in SM Sec. S4. From the figure, it can be noticed that the decay kinetics of $CsPbBr_3$/GO is faster than those of $CsPbBr_3$/RGO and $CsPbBr_3$. The respective PL maximum decay curves for all samples presented in Fig. 6(a) are nicely fitted by a triexponential function. The average lifetime for $CsPbBr_3$ is 3.9 ± 0.1 ns, which is reduced to 3.2 ± 0.1 ns for $CsPbBr_3$/RGO and 2.6 ± 0.1 for $CsPbBr_3$/GO. This reduction of lifetime

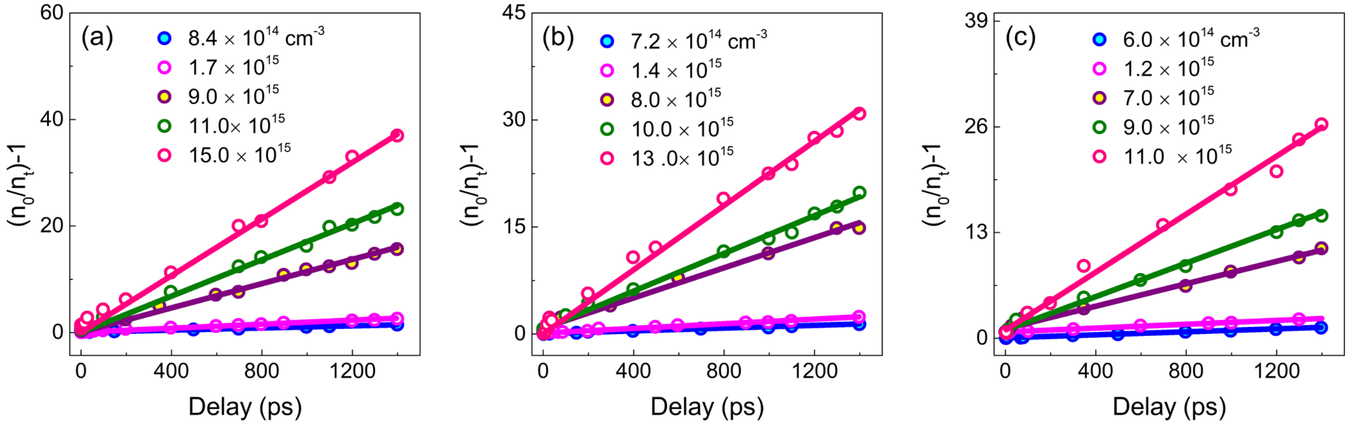

FIG. 5. Linear fit to the second-order rate equation at various fluences for (a) $CsPbBr_3$ NCs, (b) $CsPbBr_3$/RGO, and (c) $CsPbBr_3$/GO interfaces, with solid lines representing the fitted experimental data.

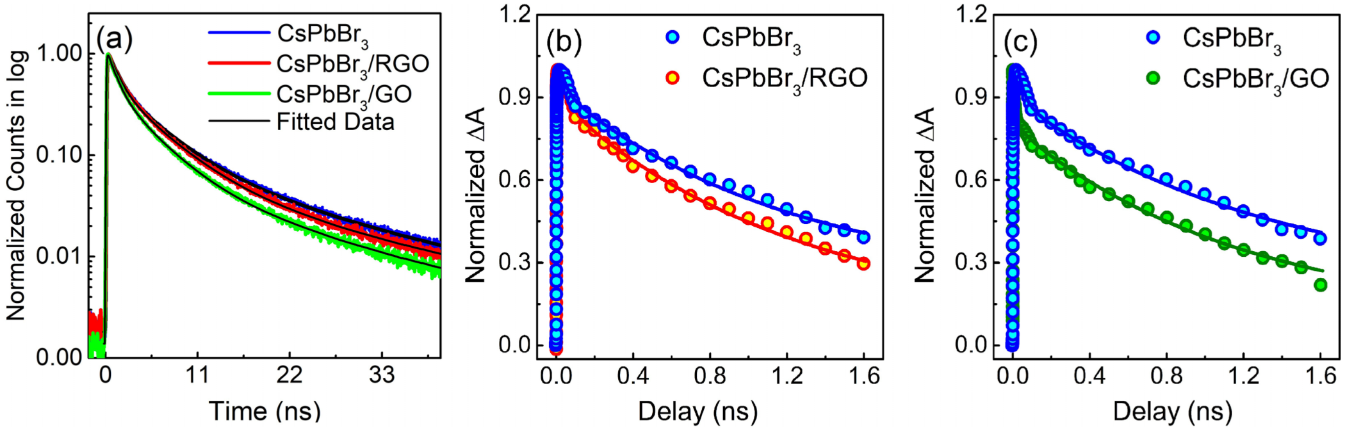

FIG. 6. (a) Normalized time-resolved PL decay kinetics of $CsPbBr_3$ NCs, $CsPbBr_3/GO$, and $CsPbBr_3/RGO$ at their respective emission maximum energies. PL decay is shown on a logarithmic scale. (b) and (c) Normalized TA decay kinetics at the bleach position for comparison of $CsPbBr_3$ NCs with $CsPbBr_3/RGO$ (b) and $CsPbBr_3/GO$ (c) interfaces at an excitation energy of 3.10 eV.

corroborates the charge transfer from $CsPbBr_3$ to GO or RGO due to strong interaction between them. This is well in agreement with the reduction of exciton (biexciton) binding energy, BGR, and suppression of Auger recombination. It is crucial to show the band structure diagram of $CsPbBr_3/GO$ and $CsPbBr_3/RGO$ to understand the charge transfer mechanism. We have presented a schematic of the band alignment of $CsPbBr_3/GO$ and $CsPbBr_3/RGO$ in Fig. S8. As shown in the figure, the VB maximum and CB minimum exist in two different materials for $CsPbBr_3/GO$, showing a type-II [62,79] band alignment. On the other hand, $CsPbBr_3/RGO$ shows a type-I band alignment [62,80], where the VB maximum and CB minimum of RGO lie inside the bands of $CsPbBr_3$ NCs. Both the band alignments indicate that the charge is transferred from $CsPbBr_3$ to GO or RGO. Since charge transfer is an ultrafast process, our time-resolved PL has a poor response at picosecond timescales; for instance, the response function of our instrument is ~100 ps. To get insight into the charge transfer time constant, we have analyzed the kinetic profile of the exciton bleach recovery from 1 to 1600 ps of $CsPbBr_3/GO$, and $CsPbBr_3/RGO$, and $CsPbBr_3$ in Figs. 6(b) and 6(c) at a fluence of 25 $\mu J/cm^2$. We have selected this time window since, by this time, the hot carriers are thermalized to the band edge. The three time constants τ_1, τ_2, and τ_3 have the values $\tau_1 = 7.0 \pm 0.4$ ps, $\tau_2 = 47 \pm 6$ ps, and $\tau_3 = 1240 \pm 19$ ps for $CsPbBr_3/GO$ and $\tau_1 = 4.2 \pm 0.1$ ps, $\tau_2 = 40 \pm 3$ ps, and $\tau_3 = 1220 \pm 22$ ps for $CsPbBr_3/RGO$. Based on previous reports, we have associated τ_2 and τ_3 with nonradiative Auger recombination and exciton radiative recombination [80,81]. Similar values of τ_2 and τ_3 ($\tau_2 = 33 \pm 4$ ps, $\tau_3 = 1213 \pm 21$ ps) are noted for $CsPbBr_3$. Notably, the incorporation of GO or RGO into $CsPbBr_3$ NCs led to the emergence of an interesting, additional short recovery channel, denoted as τ_1. This τ_1 recovery channel in $CsPbBr_3/GO$ ($CsPbBr_3/RGO$) is attributed to the efficient charge transfer from $CsPbBr_3$ to GO (RGO) with time constants of 7.0 ± 0.4 (4.2 ± 0.1) ps.

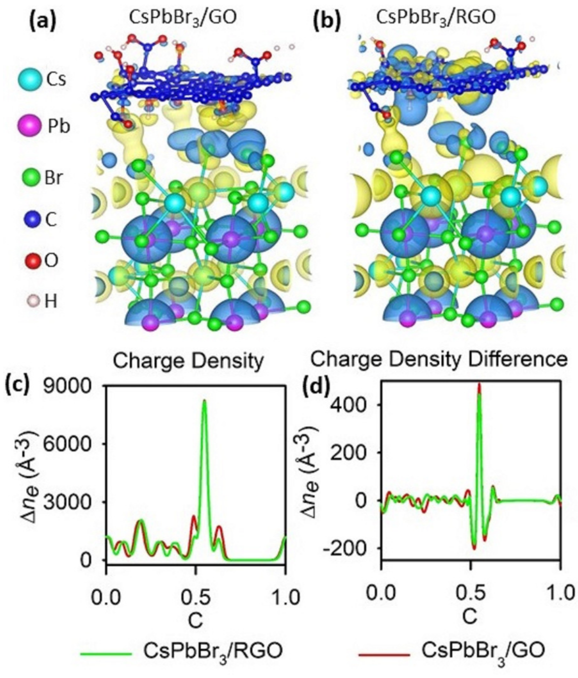

FIG. 7. Charge density difference plots at the interfaces. (a) $CsPbBr_3/GO$ and (b) $CsPbBr_3/RGO$. (c) Charge density along the z axis. (d) Charge density difference along the z axis.

D. Charge transfer between $CsPbBr_3$ and GO or RGO using first-principles calculation and Bader charge analysis

We have investigated the $CsPbBr_3/GO$ ($CsPbBr_3/RGO$) interface to understand the doping behavior and charge transfer mechanism between $CsPbBr_3$ and GO (RGO). First, we prepared the interface with $CsPbBr_3$ on top of GO (RGO), after stacking a $2 \times 2 \times 1$ supercell of $CsPbBr_3$, space group $Pm3\bar{m}$, with a $5 \times 5 \times 1$ supercell of GO (RGO). Details are in Refs. [65,81,82]. The GO or RGO structure was formed by varying concentrations of hydroxyl (OH) and carboxyl (COOH) functional ligands [83]. Finally, the construction of the interface was done by stacking these two layers using the coincidence site lattice (CSL) method, as implemented in the ATOMISTIC TOOLKIT 15.1 package [84]. The details of the CSL method are discussed in earlier reports [83,85].

Here, the mutual strain is minimized by varying the relative rotational angle between these two layers in increments of 1°. In all of our calculations, the minimized mutual strain is less than 5%, while the mutual rotational angle between the two surfaces is ∼20°. The electronic structures of $CsPbBr_3/GO$ and $CsPbBr_3/RGO$ have been investigated thoroughly using first-principles DFT calculations. $CsPbBr_3$ shows a band gap of ∼2.23 eV, as shown in Fig. S9, which is consistent with our experimental results. The VB maximum of $CsPbBr_3$ mainly consists of the Br 4*p* state, whereas the CB minimum consists of Pb 5*d* states. On the other hand, GO and RGO show heavily hybridized O 2*p* and C 2*p* states near the VB maximum or CB minimum (Fig. S9). At the $CsPbBr_3/GO$ and $CsPbBr_3/RGO$ interfaces, geometric distortions and interlayer charge transfer lead to the generation of gap states within the VB maximum and CB minimum of $CsPbBr_3$. In the $CsPbBr_3/GO$ and $CsPbBr_3/RGO$ interfaces, Pb 5*d* states have undergone a shift from +2 eV to approximately −0.3 eV (Fig. S10), keeping the 4*p* states of Br intact. The corresponding atom-projected band structures are shown in Fig. S11. The charge density difference of these systems is depicted in Figs. 7(a) and 7(b). There is a significant charge imbalance around the interface, revealing the change transfer activity between $CsPbBr_3$ and GO or RGO. Figures 7(c) and 7(d) show the charge density and charge density difference for both interfaces, respectively, along the *z* axis. The dissimilar nature of the charge along the *z* axis of the $CsPbBr_3/GO$ and $CsPbBr_3/RGO$ interfaces indicates the different doping characteristics. To quantify the charge transfer from $CsPbBr_3$ to GO or RGO, we performed Bader charge analysis, as shown in Table S2. From there, we have observed that in the $CsPbBr_3/GO$ system, there is a loss of electrons for the GO layer, which are transferred to $CsPbBr_3$ due to the formation of the interface. Therefore, in the interfacial system, holes are transferred from $CsPbBr_3$ to GO, indicating a p-type doping of the GO layer. On the other hand, for the $CsPbBr_3/RGO$ system, the RGO layer acquires electrons from the $CsPbBr_3$ layer, revealing an electron transfer from $CsPbBr_3$ to RGO and thus an n-type doping. These results are consistent with our experimental findings.

IV. CONCLUSION

In conclusion, our findings not only provide a comprehensive understanding of the many-body interactions, including the biexciton shift, BGR, and Auger process, but also explain the charge transfer dynamics in $CsPbBr_3/GO$ and $CsPbBr_3/RGO$ interfaces. TA measurements reveal that the change in the dielectric environment and the charge transfer at the interfaces lead to the reduction of the exciton and biexciton binding energies and the reduction of the BGR, respectively. Furthermore, our TA measurements demonstrate charge transfer from $CsPbBr_3$ to GO (RGO) in 7.0 ± 0.4 (4.2 ± 0.1) ps, which is an order of magnitude faster than previously reported other acceptor layers. These results indicate that GO or RGO can serve as an excellent acceptor and can be utilized as a transparent conducting layer material. Overall, our systematic studies provide a future direction for developing advanced perovskite-based interface designs for several optoelectronic and photovoltaic applications.

ACKNOWLEDGMENTS

The authors gratefully acknowledge the Science and Engineering Research Board (Project No. CRG/2019/002808), DAE BRNS [Sanction No. 37(3)/14/26/2016-BRNS/37245], and the FIST Project (Project No. PSI-195/2014) for the Department of Physics. D.K. acknowledges the BARC ANUPAM supercomputing facility. N.C.M. gratefully acknowledges INSPIRE-DST for financial assistance. S.K.B. acknowledges the Ministry of Education for support from the Prime Minister's Research Fellowship. D.M. and M.N.H. acknowledge CSIR fellowships for financial support.

---

[1] M. V. Kovalenko, L. Protesescu, and M. I. Bodnarchuk, Properties and potential optoelectronic applications of lead halide perovskite nanocrystals, Science **358**, 745 (2017).

[2] J. Hao and X. Xiao, Recent development of optoelectronic application based on metal halide perovskite nanocrystals, Front. Chem. **9**, 822106 (2022).

[3] J. Butkus, P. Vashishtha, K. Chen, J. K. Gallaher, S. K. K. Prasad, D. Z. Metin, G. Laufersky, N. Gaston, J. E. Halpert, and J. M. Hodgkiss, The evolution of quantum confinement in $CsPbBr_3$ perovskite nanocrystals, Chem. Mater. **29**, 3644 (2017).

[4] W. Du, S. Zhang, Q. Zhang, and X. Liu, Recent progress of strong exciton-photon coupling in lead halide perovskites, Adv. Mater. **31**, 1804894 (2019).

[5] A. Dutta, R. K. Behera, P. Pal, S. Baitalik, and N. Pradhan, Near-unity photoluminescence quantum efficiency for all $CsPbX_3$ (X=Cl, Br, and I) perovskite nanocrystals: A generic synthesis approach, Angew. Chem. Int. Ed. **58**, 5552 (2019).

[6] M. A. Becker, R. Vaxenburg, G. Nedelcu, P. C. Sercel, A. Shabaev, M. J. Mehl, J. G. Michopoulos, S. G. Lambrakos, N. Bernstein, J. L. Lyons, T. Stöferle, R. F. Mahrt, M. V. Kovalenko, D. J. Norris, G. Rainò, and A. L. Efros, Bright triplet excitons in caesium lead halide perovskites, Nature (London) **553**, 189 (2018).

[7] Q. A. Akkerman, G. Rainó, M. V. Kovalenko, and L. Manna, Genesis, challenges and opportunities for colloidal lead halide perovskite nanocrystals, Nat. Mater. **17**, 394 (2018).

[8] D. Shi, V. Adinolfi, R. Comin, M. Yuan, E. Alarousu, A. Buin, Y. Chen, S. Hoogland, A. Rothenberger, K. Katsiev, Y. Losovyj, X. Zhang, P. A. Dowben, O. F. Mohammed, E. H. Sargent, and O. M. Bakr, Low trap-state density and long carrier diffusion in organolead trihalide perovskite single crystals, Science **347**, 519 (2015).

[9] S. D. Stranks and H. J. Snaith, Metal-halide perovskites for photovoltaic and light-emitting devices, Nat. Nanotechnol. **10**, 391 (2015).

[10] G. R. Yettapu, D. Talukdar, S. Sarkar, A. Swarnkar, A. Nag, P. Ghosh, and P. Mandal, Terahertz conductivity within colloidal $CsPbBr_3$ perovskite nanocrystals: Remarkably high carrier mobilities and large diffusion lengths, Nano Lett. **16**, 4838 (2016).

[11] D. Rossi, X. Liu, Y. Lee, M. Khurana, J. Puthenpurayil, K. Kim, A. V. Akimov, J. Cheon, and D. H. Son, Intense dark exciton emission from strongly quantum-confined $CsPbBr_3$ nanocrystals, Nano Lett. **20**, 7321 (2020).

[12] S. Yakunin, L. Protesescu, F. Krieg, M. I. Bodnarchuk, G. Nedelcu, M. Humer, G. De Luca, M. Fiebig, W. Heiss, and M. V. Kovalenko, Low-threshold amplified spontaneous emission and lasing from colloidal nanocrystals of caesium lead halide perovskites, Nat. Commun. **6**, 8056 (2015).

[13] J. Song, J. Li, X. Li, L. Xu, Y. Dong, and H. Zeng, Quantum dot light-emitting diodes based on inorganic perovskite cesium lead halides ($CsPbX_3$), Adv. Mater. **27**, 7162 (2015).

[14] D. P. McMeekin, G. Sadoughi, W. Rehman, G. E. Eperon, M. Saliba, M. T. Hörantner, A. Haghighirad, N. Sakai, L. Korte, B. Rech, M. B. Johnston, L. M. Herz, and H. J. Snaith, A mixed-cation lead mixed-halide perovskite absorber for tandem solar cells, Science **351**, 151 (2016).

[15] V. V. Belykh, D. R. Yakovlev, M. M. Glazov, P. S. Grigoryev, M. Hussain, J. Rautert, D. N. Dirin, M. V. Kovalenko, and M. Bayer, Coherent spin dynamics of electrons and holes in $CsPbBr_3$ perovskite crystals, Nat. Commun. **10**, 673 (2019).

[16] S. McKechnie, J. M. Frost, D. Pashov, P. Azarhoosh, A. Walsh, and M. van Schilfgaarde, Dynamic symmetry breaking and spin splitting in metal halide perovskites, Phys. Rev. B **98**, 085108 (2018).

[17] M. Shrivastava, M. I. Bodnarchuk, A. Hazarika, J. M. Luther, M. C. Beard, M. V. Kovalenko, and K. V. Adarsh, Polaron and spin dynamics in organic-inorganic lead halide perovskite nanocrystals, Adv. Opt. Mater. **8**, 2001016 (2020).

[18] A. K. Poonia, M. Shrivastava, W. J. Mir, J. Aneesh, A. Nag, and K. V. Adarsh, Intervalley polaronic biexcitons in metal halide perovskite quantum dots, Phys. Rev. B **104**, L161407 (2021).

[19] M. Shrivastava, A. Hazarika, J. Aneesh, D. Mandal, M. C. Beard, and K. V. Adarsh, Giant spin-selective bandgap renormalization in $CsPbBr_3$ colloidal nanocrystals, Phys. Rev. B **106**, L041404 (2022).

[20] G. Yumoto, H. Hirori, F. Sekiguchi, R. Sato, M. Saruyama, T. Teranishi, and Y. Kanemitsu, Strong spin-orbit coupling inducing Autler-Townes effect in lead halide perovskite nanocrystals, Nat. Commun. **12**, 3026 (2021).

[21] V. Klimov, S. Hunsche, and H. Kurz, Biexciton effects in femtosecond nonlinear transmission of semiconductor quantum dots, Phys. Rev. B **50**, 8110 (1994).

[22] D. P. Strandell and P. Kambhampati, Observing strongly confined multiexcitons in bulk-like $CsPbBr_3$ nanocrystals, J. Chem. Phys. **158**, 154702 (2023).

[23] N. Yoshikawa, H. Hirori, H. Watanabe, T. Aoki, T. Ihara, R. Kusuda, C. Wolpert, T. K. Fujiwara, A. Kusumi, Y. Kanemitsu, and K. Tanaka, Biexciton state causes photoluminescence fluctuations in CdSe/ZnS core/shell quantum dots at high photoexcitation densities, Phys. Rev. B **88**, 155440 (2013).

[24] H. Tahara, M. Sakamoto, T. Teranishi, and Y. Kanemitsu, Harmonic quantum coherence of multiple excitons in PbS/CdS core-shell nanocrystals, Phys. Rev. Lett. **119**, 247401 (2017).

[25] H. Tahara, M. Sakamoto, T. Teranishi, and Y. Kanemitsu, Quantum coherence of multiple excitons governs absorption cross-sections of PbS/CdS core/shell nanocrystals, Nat. Commun. **9**, 3179 (2018).

[26] J. A. Castañeda, G. Nagamine, E. Yassitepe, L. G. Bonato, O. Voznyy, S. Hoogland, A. F. Nogueira, E. H. Sargent, C. H. B. Cruz, and L. A. Padilha, Efficient biexciton interaction in perovskite quantum dots under weak and strong confinement, ACS Nano **10**, 8603 (2016).

[27] J. Singh, D. Birkedal, V. G. Lyssenko, and J. M. Hvam, Binding energy of two-dimensional biexcitons, Phys. Rev. B **53**, 15909 (1996).

[28] D. Birkedal, J. Singh, V. G. Lyssenko, J. Erland, and J. M. Hvam, Binding of quasi-two-dimensional biexcitons, Phys. Rev. Lett. **76**, 672 (1996).

[29] Y. You, X.-X. Zhang, T. C. Berkelbach, M. S. Hybertsen, D. R. Reichman, and T. F. Heinz, Observation of biexcitons in monolayer WSe_2, Nat. Phys. **11**, 477 (2015).

[30] Y. Yang, D. P. Ostrowski, R. M. France, K. Zhu, J. van de Lagemaat, J. M. Luther, and M. C. Beard, Observation of a hot-phonon bottleneck in lead-iodide perovskites, Nat. Photonics **10**, 53 (2016).

[31] R. Su, Z. Xu, J. Wu, D. Luo, Q. Hu, W. Yang, X. Yang, R. Zhang, H. Yu, T. P. Russell, Q. Gong, W. Zhang, and R. Zhu, Dielectric screening in perovskite photovoltaics, Nat. Commun. **12**, 2479 (2021).

[32] V. A. Hintermayr, L. Polavarapu, A. S. Urban, and J. Feldmann, Accelerated carrier relaxation through reduced Coulomb screening in two-dimensional halide perovskite nanoplatelets, ACS Nano **12**, 10151 (2018).

[33] Y. Yang, M. Yang, K. Zhu, J. C. Johnson, J. J. Berry, J. Van De Lagemaat, and M. C. Beard, Large polarization-dependent exciton optical Stark effect in lead iodide perovskites, Nat. Commun. **7**, 12613 (2016)

[34] C. Jin, E. Y. Ma, O. Karni, E. C. Regan, F. Wang, and T. F. Heinz, Ultrafast dynamics in van der Waals heterostructures, Nat. Nanotechnol. **13**, 994 (2018).

[35] A. Raja, A. Chaves, J. Yu, G. Arefe, H. M. Hill, A. F. Rigosi, T. C. Berkelbach, P. Nagler, C. Schüller, T. Korn, C. Nuckolls, J. Hone, L. E. Brus, T. F. Heinz, D. R. Reichman, and A. Chernikov, Coulomb engineering of the bandgap and excitons in two-dimensional materials, Nat. Commun. **8**, 15251 (2017).

[36] A. Chernikov, C. Ruppert, H. M. Hill, A. F. Rigosi, and T. F. Heinz, Population inversion and giant bandgap renormalization in atomically thin WS_2 layers, Nat. Photonics **9**, 466 (2015).

[37] S. K. Bera, M. Shrivastava, K. Bramhachari, H. Zhang, A. K. Poonia, D. Mandal, E. M. Miller, M. C. Beard, A. Agarwal, and K. V. Adarsh, Atomlike interaction and optically tunable giant band-gap renormalization in large-area atomically thin MoS_2, Phys. Rev. B **104**, L201404 (2021).

[38] N. S. Makarov, S. Guo, O. Isaienko, W. Liu, I. Robel, and V. I. Klimov, Spectral and dynamical properties of single excitons, biexcitons, and trions in cesium-lead-halide perovskite quantum dots, Nano Lett. **16**, 2349 (2016).

[39] H. Utzat, W. Sun, A. E. K. Kaplan, F. Krieg, M. Ginterseder, B. Spokoyny, N. D. Klein, K. E. Shulenberger, C. F. Perkinson, M. V. Kovalenko, and M. G. Bawendi, Coherent single-photon emission from colloidal lead halide perovskite quantum dots, Science **363**, 1068 (2019).

[40] J.-W. Lee, D.-H. Kim, H.-S. Kim, S.-W. Seo, S. M. Cho, and N.-G. Park, Formamidinium and cesium hybridization for photo-and moisture-stable perovskite solar cell, Adv. Energy Mater. **5**, 1501310 (2015).

[41] A. Hazarika, Q. Zhao, E. A. Gaulding, J. A. Christians, B. Dou, A. R. Marshall, T. Moot, J. J. Berry, J. C. Johnson, and J. M. Luther, Perovskite quantum dot photovoltaic materials beyond

the reach of thin films: Full-range tuning of A-site cation composition, ACS Nano **12**, 10327 (2018).

[42] L. A. Frolova, Q. Chang, S. Yu. Luchkin, D. Zhao, A. F. Akbulatov, N. N. Dremova, A. V. Ivanov, E. E. M. Chia, K. J. Stevenson, and P. A. Troshin, Efficient and stable all-inorganic perovskite solar cells based on nonstoichiometric $Cs_xPbI_2Br_x$ ($x > 1$) alloys, J. Mater. Chem. C **7**, 5314 (2019).

[43] A. Pan, B. He, X. Fan, Z. Liu, J. J. Urban, A. P. Alivisatos, L. He, and Y. Liu, Insight into the ligand-mediated synthesis of colloidal $CsPbBr_3$ perovskite nanocrystals: The role of organic acid, base, and cesium precursors, ACS Nano **10**, 7943 (2016).

[44] S. K. Bera, S. Bera, M. Shrivastava, N. Pradhan, and K. V. Adarsh, Facet engineering for amplified spontaneous emission in metal halide perovskite nanocrystals, Nano Lett. **22**, 8908 (2022).

[45] L. Lin, L. Qiu, F. Li, C. You, Y. Zhu, Q. Yao, Y. Zeng, Y. Wang, J. Li, and X. Chen, Stable electrochemiluminescence of $CsPbBr_3$ perovskite nanocrystals assisted by graphene oxide for ultrasensitive sensing, ACS Appl. Nano Mater. **4**, 8823 (2021).

[46] S. Zhang, R. Guo, H. Zeng, Y. Zhao, X. Liu, S. You, M. Li, L. Luo, M. Lira-Cantu, L. Li, F. Liu, X. Zheng, G. Liao, and X. Li, Improved performance and stability of perovskite solar modules by interface modulating with graphene oxide crosslinked $CsPbBr_3$ quantum dots, Energy Environ. Sci. **15**, 244 (2022).

[47] X. Tang, Z. Zu, Z. Zang, Z. Hu, W. Hu, Z. Yao, W. Chen, S. Li, S. Han, and M. Zhou, $CsPbBr_3$/reduced graphene oxide nanocomposites and their enhanced photoelectric detection application, Sens. Actuators B **245**, 435 (2017).

[48] Y. F. Xu, M. Z. Yang, B. X. Chen, X. D. Wang, H. Y. Chen, D. B. Kuang, and C. Y. Su, A $CsPbBr_3$ perovskite quantum dot/graphene oxide composite for photocatalytic CO_2 reduction, J. Am. Chem. Soc. **139**, 5660 (2017).

[49] Y. H. Chen, J. K. Ye, Y. J. Chang, T. W. Liu, Y. H. Chuang, W. R. Liu, S. H. Liu, and Y. C. Pu, Mechanisms behind photocatalytic CO_2 reduction by $CsPbBr_3$ perovskite-graphene-based nanoheterostructures, Appl. Catal. B **284**, 119751 (2021).

[50] W. Zhang, D. Luo, S.-F. Ni, S. Chen, L. Cha, M.-D. Li, and L. Dang, Ultrafast carrier dynamics study on graphene oxide-$CsPbBr_3$ nanocomposites, J. Phys. Chem. C **127**, 10680 (2023).

[51] S. Muduli, P. Pandey, G. Devatha, R. Babar, T. M, D. C. Kothari, M. Kabir, P. P. Pillai, and S. Ogale, Photoluminescence quenching in self-assembled $CsPbBr_3$ quantum dots on few-layer black phosphorus sheets, Angew. Chem. Int. Ed. **57**, 7682 (2018).

[52] M. T. Hossain, M. Das, J. Ghosh, S. Ghosh, and P. K. Giri, Understanding the interfacial charge transfer in the CVD grown $Bi_2O_2Se/CsPbBr_3$ nanocrystal heterostructure and its exploitation in superior photodetection: Experiment vs. theory, Nanoscale **13**, 14945 (2021).

[53] R. Karmakar, D. Sen, D. Mandal, and K. V. Adarsh, Ultrafast charge-transfer mediated indirect-excitons in $CsPbBr_3/MoS_2$ heterostructure, in *Conference on Lasers and Electro-Optics* (Optica, San Jose, CA, 2021), paper No. JW1A.100.

[54] P. N. Immanuel, S. J. Huang, V. Danchuk, A. Sedova, J. Prilusky, A. Goldreich, H. Shalom, A. Musin, and L. Yadgarov, Improving the stability of halide perovskite solar cells using nanoparticles of tungsten disulfide, Nanomaterials **12**, 4454 (2022).

[55] P. N. Immanuel, S. J. Huang, P. Taank, A. Goldreich, J. Prilusky, A. Byregowda, R. Carmiel, A. Zak, N. Aggarwal, K. V. Adarsh, and L. Yadgarov, Enhanced photocatalytic activity of Cs_4PbBr_6/WS_2 hybrid nanocomposite, ChemRxiv, doi:10.26434/chemrxiv-2022-gxmvh.

[56] A. De, S. Das, and A. Samanta, Hot hole transfer dynamics from $CsPbBr_3$ perovskite nanocrystals, ACS Energy Lett. **5**, 2246 (2020).

[57] G. Ghosh, K. Marjit, S. Ghosh, A. Ghosh, R. Ahammed, A. De Sarkar, and A. Patra, Hot hole cooling and transfer dynamics from lead halide perovskite nanocrystals using porphyrin molecules, J. Phys. Chem. C **125**, 5859 (2021).

[58] A. De, N. Mondal, and A. Samanta, Hole transfer dynamics from photoexcited cesium lead halide perovskite nanocrystals: 1-Aminopyrene as hole acceptor, J. Phys. Chem. C **122**, 13617 (2018).

[59] S. Sarkar, V. K. Ravi, S. Banerjee, G. R. Yettapu, G. B. Markad, A. Nag, and P. Mandal, Terahertz spectroscopic probe of hot electron and hole transfer from colloidal $CsPbBr_3$ perovskite nanocrystals, Nano Lett. **17**, 5402 (2017).

[60] R. A. Scheidt, E. Kerns, and P. V. Kamat, Interfacial charge transfer between excited $CsPbBr_3$ nanocrystals and TiO_2: Charge injection versus photodegradation, J. Phys. Chem. Lett. **9**, 5962 (2018).

[61] S. Mandal, L. George, and N. V. Tkachenko, Charge transfer dynamics in $CsPbBr_3$ perovskite quantum dots-anthraquinone/fullerene (C_{60}) hybrids, Nanoscale **11**, 862 (2019).

[62] V. K. Ravi, G. B. Markad, and A. Nag, Band edge energies and excitonic transition probabilities of colloidal $CsPbX_3$ (X = Cl, Br, I) perovskite nanocrystals, ACS Energy Lett. **1**, 665 (2016).

[63] D. C. Marcano, D. V. Kosynkin, J. M. Berlin, A. Sinitskii, Z. Sun, A. Slesarev, L. B. Alemany, W. Lu, and J. M. Tour, Improved synthesis of graphene oxide, ACS Nano **4**, 4806 (2010).

[64] R. K. Yadav, J. Aneesh, R. Sharma, P. Abhiramnath, T. K. Maji, G. J. Omar, A. K. Mishra, D. Karmakar, and K. V. Adarsh, Designing hybrids of graphene oxide and gold nanoparticles for nonlinear optical response, Phys. Rev. Appl. **9**, 044043 (2018).

[65] See Supplemental Material at http://link.aps.org/supplemental/10.1103/PhysRevB.108.155417 for details of the sample preparation, basic physical characterizations, Elliott's hydrogenic Wannier-Mott exciton model, experimental methods, schematic diagrams of the band alignment, computational details, and fitting parameters.

[66] R. J. Elliott, Intensity of optical absorption by excitons, Phys. Rev. **108**, 1384 (1957).

[67] A. E. M. Abd Elhamid, H. Shawkey, A. A. Nada, and M. Bechelany, Anomalous dielectric constant value of graphene oxide/polyvinyl alcohol thin film, Solid State Sci. **94**, 28 (2019).

[68] J. Liu, D. Galpaya, M. Notarianni, C. Yan, and N. Motta, Graphene-based thin film supercapacitor with graphene oxide as dielectric spacer, Appl. Phys. Lett. **103**, 063108 (2013).

[69] K. S. Kumar, S. Pittala, S. Sanyadanam, and P. Paik, A new single/few-layered graphene oxide with a high dielectric constant of 10^6: Contribution of defects and functional groups, RSC Adv. **5**, 14768 (2015).

[70] C. Yuwen, B. Liu, L. Zhang, S. Guo, and J. Peng, Synthesis high-quality graphene oxide and temperature-dependent dielectric properties of reduced graphene oxide, Mater. Res. Express **6**, 0950b4 (2019).

[71] M. N. Almadhoun, M. N. Hedhili, I. N. Odeh, P. Xavier, U. S. Bhansali, and H. N. Alshareef, Influence of stacking

morphology and edge nitrogen doping on the dielectric performance of graphene-polymer nanocomposites, Chem. Mater. **26**, 2856 (2014).

[72] I. V. Lightcap and P. V. Kamat, Fortification of CdSe quantum dots with graphene oxide. Excited state interactions and light energy conversion, J. Am. Chem. Soc. **134**, 7109 (2012).

[73] P. Taank, R. Karmakar, R. Sharma, R. K. Yadav, M. Shrivastava, N. C. Maurya, T. K. Maji, D. Karmakar, and K. V. Adarsh, An insightful picture of multi-particle recombination in few-layer MoS_2 nanosheets, J. Phys. Chem. C **126**, 416 (2022).

[74] G. Yumoto, H. Tahara, T. Kawawaki, M. Saruyama, R. Sato, T. Teranishi, and Y. Kanemitsu, Hot biexciton effect on optical gain in $CsPbI_3$ perovskite nanocrystals, J. Phys. Chem. Lett. **9**, 2222 (2018).

[75] A. Mondal, J. Aneesh, V. Kumar Ravi, R. Sharma, W. J. Mir, M. C. Beard, A. Nag, and K. V. Adarsh, Ultrafast exciton many-body interactions and hot-phonon bottleneck in colloidal cesium lead halide perovskite nanocrystals, Phys. Rev. B **98**, 115418 (2018).

[76] J. Aneesh, A. Swarnkar, V. Kumar Ravi, R. Sharma, A. Nag, and K. V. Adarsh, Ultrafast exciton dynamics in colloidal $CsPbBr_3$ perovskite nanocrystals: Biexciton effect and auger recombination, J. Phys. Chem. C **121**, 4734 (2017).

[77] J. S. Manser and P. V. Kamat, Band filling with free charge carriers in organometal halide perovskites, Nat. Photonics **8**, 737 (2014).

[78] *Advanced Time-Correlated Single Photon Counting Applications*, edited by W. Becker (Springer International, Cham, Switzerland, 2015).

[79] K. H. Tu, S. S. Li, W. C. Li, D. Y. Wang, J. R. Yang, and C. W. Chen, Solution processable nanocarbon platform for polymer solar cells, Energy Environ. Sci. **4**, 3521 (2011).

[80] Y. Zhang, J. Du, Z. Wang, M. Luo, Y. Tian, T. Fujita, Q. Xue, and M. Chen, Three-dimensional nanoporous heterojunction of monolayer MoS_2@rGO for photoenhanced hydrogen evolution reaction, ACS Appl. Energy Mater. **1**, 2183 (2018).

[81] G. Kresse and J. Furthmüller, Efficient iterative schemes for *ab initio* total-energy calculations using a plane-wave basis set, Phys. Rev. B **54**, 11169 (1996).

[82] S. Grimme, Semiempirical GGA-type density functional constructed with a long-range dispersion correction, J. Comput. Chem. **27**, 1787 (2006).

[83] T. K. Maji, K. Vaibhav, S. K. Pal, K. Majumdar, K. V. Adarsh, and D. Karmakar, Intricate modulation of interlayer coupling at the graphene oxide/$MoSe_2$ interface: Application in time-dependent optics and device transport, Phys. Rev. B **99**, 115309 (2019).

[84] S. Smidstrup, D. Stradi, J. Wellendorff, P. A. Khomyakov, U. G. Vej-Hansen, M.-E. Lee, T. Ghosh, E. Jónsson, H. Jónsson, and K. Stokbro, First-principles Green's-function method for surface calculations: A pseudopotential localized basis set approach, Phys. Rev. B **96**, 195309 (2017).

[85] T. K. Maji, A. J. R, S. Mukherjee, R. Alexander, A. Mondal, S. Das, R. K. Sharma, N. K. Chakraborty, K. Dasgupta, A. M. R. Sharma, R. Hawaldar, M. Pandey, A. Naik, K. Majumdar, S. K. Pal, K. V. Adarsh, S. K. Ray, and D. Karmakar, Combinatorial large-area MoS_2/anatase-TiO_2 interface: A pathway to emergent optical and optoelectronic functionalities, ACS Appl. Mater. Interfaces **12**, 44345 (2020).